Micromachined Integrated Quantum Circuit Containing a Superconducting Qubit

T. Brecht,* Y. Chu, C. Axline, W. Pfaff, J. Z. Blumoff, K. Chou, L. Krayzman, L. Frunzio, and R. J. Schoelkopf

Department of Applied Physics, Yale University, New Haven, Connecticut 06511, USA
and Yale Quantum Institute, Yale University, New Haven, Connecticut 06520, USA

(Received 14 November 2016; revised manuscript received 6 February 2017; published 19 April 2017)

We present a device demonstrating a lithographically patterned transmon integrated with a micromachined cavity resonator. Our two-cavity, one-qubit device is a multilayer microwave-integrated quantum circuit (MMIQC), comprising a basic unit capable of performing circuit-QED operations. We describe the qubit-cavity coupling mechanism of a specialized geometry using an electric-field picture and a circuit model, and obtain specific system parameters using simulations. Fabrication of the MMIQC includes lithography, etching, and metallic bonding of silicon wafers. Superconducting wafer bonding is a critical capability that is demonstrated by a micromachined storage-cavity lifetime of 34.3 μs, corresponding to a quality factor of 2×10^6 at single-photon energies. The transmon coherence times are $T_1 = 6.4$ μs, and $T_2^{\text{echo}} = 11.7$ μs. We measure qubit-cavity dispersive coupling with a rate $\chi_{q\mu}/2\pi = -1.17$ MHz, constituting a Jaynes-Cummings system with an interaction strength $g/2\pi = 49$ MHz. With these parameters we are able to demonstrate circuit-QED operations in the strong dispersive regime with ease. Finally, we highlight several improvements and anticipated extensions of the technology to complex MMIQCs.

DOI: 10.1103/PhysRevApplied.7.044018

I. INTRODUCTION

Quantum circuits are quickly reaching a size and complexity that puts extreme demands on input-output connections as well as selective isolation among internal elements. Continued progress will require 3D integration and rf packaging techniques [1,2] that allow for scaling. Indeed, there are numerous developed technologies waiting to see fruitful implementation in the field of circuit-QED (cQED) operations, both from room temperature microwave devices [3,4] and complex superconducting circuits [5–7]. To address this opportunity and the associated challenges for quantum coherence, we recently proposed the multilayer microwave-integrated quantum circuit (MMIQC) architecture [8], which adapts many existing circuit design and fabrication techniques to cQED. A crucial step towards this vision is the demonstration of superconducting micromachined cavities [9], which can be used as quantum memories or as shielding enclosures to prevent cross-talk in more complex quantum computing devices. However, integrating transmons into these micromachined cavities has yet to be discussed, and is not a trivial matter of replicating the common methods in either existing planar or 3D cQED circuits. Fortunately, the flexibility and durability of MMIQC hardware affords many possibilities for qubit integration.

In this work, we demonstrate one such possibility through the design, fabrication, and characterization of a quantum device containing a transmon qubit coupled to a superconducting micromachined cavity. It forms a simple MMIQC capable of performing cQED operations. The techniques shown here can be improved and extended to realize more complex quantum circuitry.

II. QUBIT-RESONATOR COUPLING

Coupling between an electromagnetic resonator and a transmon occurs via shared electric and magnetic fields of their respective modes. Both planar circuits and 3D qubits use a simple dipole antenna structure aligned with the electric field of a transmission line, waveguide, or cavity [10]. These common schemes are diagrammed in Figs. 1(a) and 1(b). It would be impractical to use a similar scheme for coupling qubits to micromachined cavities because of the extreme aspect ratio imposed by the wafer height. Instead, we desire to achieve the same coupling while limiting ourselves to planar fabrication and wafer stacking. A circuit can be patterned on one of the cavity walls such that the electromagnetic fields couple to those of the cavity, as shown in Fig. 1(c).

The coupling of an "aperture transmon" to a resonator using fields that are out of the plane of transmon fabrication is described in Ref. [11]. In the device of the present work, the coupling can be understood by analyzing the overlap between the electric fields of the transmon mode and those of the adjacent cavity mode(s), and also by an equivalent circuit model. Translation of the aperture transmon away from the center of the cavity wall results in a mixture of electric (charge accumulation) and magnetic (current flow)

*teresa.brecht@yale.edu

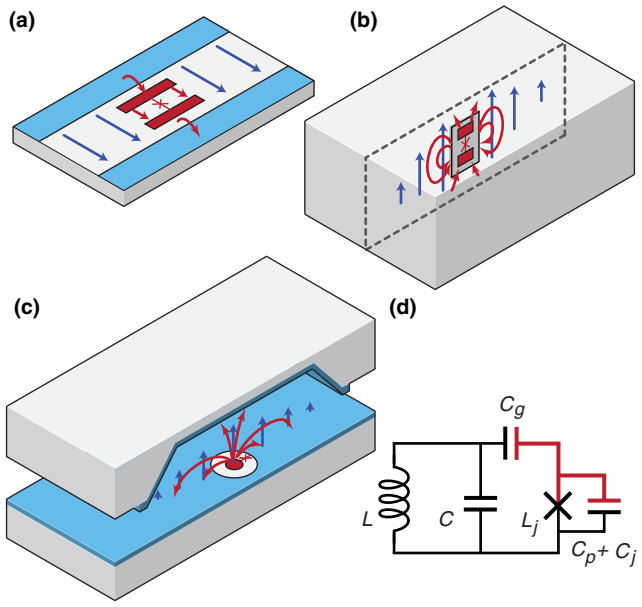

FIG. 1. Illustrations of dipole coupling in cQED. Electric dipole-moment orientations for typical transmons are fabricated to align with (a) the electric field of a planar transmission line resonator or (b) the electric field of an encapsulating 3D cavity. Blue arrows show electric-field lines of the each resonator's fundamental mode, and red arrows show electric-field lines of the transmon mode. (c) The aperture transmon fields couple to the fundamental mode of the micromachined cavity in the device discussed in this work. For clarity, the diagram shows an exploded cross-sectional view of two substrate wafers, and it is not to scale. (d) Schematic circuit diagram of the aperture transmon and electromagnetic resonator. The red coloring corresponds to the central island.

coupling. However, the aperture transmon's central location maximizes total coupling.

The schematic circuit diagram is depicted in Fig. 1(d). A single Josephson junction connects the central island to the rest of the cavity wall. It is accompanied by a junction capacitance (C_j), which is small compared to the other capacitors in the system: First, there is a capacitance across the open annulus between the island and the rest of the lower cavity wall (C_p). Second, there is a capacitance across the gap between the island and the opposite wall of the cavity (C_g). Last, there is capacitance C associated with the walls of the cavity, which combines with an effective inductance L to create the LC-resonator characteristic of the cavity's fundamental mode at frequency $\omega_\mu/2\pi$.

The system of qubit excitations and resonator photons displays a Jaynes-Cummings interaction: $\hbar g(a^\dagger\sigma^- + a\sigma^+)$, where $a^\dagger(a)$ creates (annihilates) a photon and $\sigma^+(\sigma^-)$ creates (annihilates) an excitation of the qubit. The coupling rate $g = eV_0\beta/\hbar$ is a function of the capacitances, $\beta = C_g/(C_g + C_p + C_j)$, and $V_0 = \sqrt{\hbar\omega_\mu/2C}$. This circuit picture using capacitances reveals the relationships between device geometry and coupling strength, analogous to other cQED hardware designs [12]. See Supplemental Material for details [13]. In this work, we operate such a system in the strong dispersive limit, where the frequency detuning between resonator and qubit is much greater than the interaction rate ($|\Delta| \gg g$) and the interaction rate is much greater than the decay rates of the qubit or cavity ($g \gg \gamma, \kappa$).

In this strong dispersive limit, we approximate the applicable Hamiltonian as

$$\frac{H}{\hbar} = \sum_i \omega_i a_i^\dagger a_i - \sum_{i\neq j} \chi_{ij} a_i^\dagger a_i a_j^\dagger a_j - \sum_i \frac{\alpha_i}{2} a_i^{\dagger 2} a_i^2 \qquad (1)$$

including an arbitrary number of modes. Each mode has a transition frequency ω_i between its first two levels and an anharmonicity α_i, which is greatest for the transmon. Each pair of modes interacts via a dispersive shift of strength χ_{ij}.

III. DEVICE IMPLEMENTATION

The first MMIQC prototype is designed to have coherent quantum modes that have sufficient coupling rates between them, and allow for manipulation and measurement with microwave pulses. The device featured in this work consists of three quantum objects. An aperture transmon couples simultaneously to two cavity modes. In addition to a micromachined cavity, a second cavity made by traditional metal machining is incorporated to compose a two-cavity–one-qubit MMIQC device. This cavity allows a readout of the transmon and micromachined cavity states through two pins leading to coaxial cables for microwave access to the system, and is hereafter referred to as the "readout cavity." The device, shown in Fig. 2, displays a hybrid multilayer construction, including silicon wafers and conventionally machined metals united by indium bonding on flat surfaces. The integration of the machined 3D cavity demonstrates the aperture transmon's bipartite coupling and provides a convenient way of applying connectors.

Next, we must choose design parameters to realize the MMIQC. We also impose that the qubit is in the transmon regime, with suppressed charge dispersion [19,20]. The shape and position of the aperture transmon affect properties of the system between which trade-offs are considered. For example, the size of the inner island must be large enough to create a measurable g by the capacitance contribution C_g. However, if the inner island is too large, the anharmonicity is reduced, limiting the speed of manipulation pulses. Scaling trends of g changing with respect to several relevant geometrical parameters are included in the Supplemental Material [13–15]. The coupling between the qubit and the micromachined cavity $\chi_{q\mu}$ and that of the qubit and the readout cavity χ_{qr} are also adjusted by the choice of heights of each cavity and thickness of the qubit substrate. We perform simulations in order to confirm our understanding

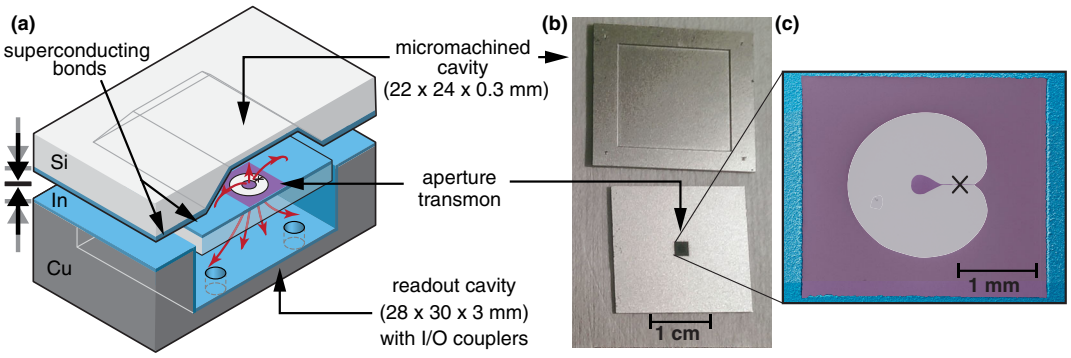

FIG. 2. (a) Sketch of device. For clarity, the image shows an exploded cross-sectional view that is not to scale. The annular structure has electric dipole-moment components in two opposing directions, both perpendicular to the plane of fabrication. Red arrows show electric-field lines of the transmon mode, and the transmon chip is shown semitransparent. (b) Photograph of the micromachined cavity chip (top) and transmon chip (bottom). (c) False-colored SEM image of the aperture transmon, with silicon in gray, aluminum in purple, and indium in blue. The shape of the electrodes is described in the Supplemental Material [13]. An "X" indicates the Josephson-junction position, interrupting a 50-μm-wide lead connecting the inner island to the remainder of the cavity wall.

of the qubit-cavity coupling and to aid geometry optimization more precisely. We model the entire system using a full 3D electromagnetic simulation using a finite element solver followed by black-box quantization analysis [21]. For the design featured in this work, the anharmonicity is designed to be $\alpha_q = -E_c = -204$ MHz, and the Josephson energy is $E_J/h = \Phi_0^2 L_J/2\pi h = 39$ GHz. ($E_J/E_C = 193$.)

We now briefly describe how the device is constructed. The multilayer device is fabricated as three separate parts [see Fig. 2(a)] that are finally bonded together with a metal that superconducts. The micromachined cavity chip is created by wet etching a rectangular pit to a depth of 300 μm in silicon, followed by metallization with 10 μm of indium [9,13]. The transmon chip requires three metallization steps on a 325-μm-thick silicon wafer: a patterning of gold by liftoff, electron-beam lithography, and shadow angle evaporation of the aluminum Josephson junction, and masking this junction before electroplating 10 μm of indium onto the gold. The readout cavity is milled out of oxygen-free high-conductivity copper and electroplated with 30 μm of indium. The three components are bonded together between parallel plates at 120 °C in two steps. Once assembled, coaxial pin couplers are added to the readout cavity and the device is thermally anchored to the baseplate of a dilution refrigerator reaching a base temperature of 15 mK. See the Supplemental Material [13,17,18] for additional fabrication and bonding details.

IV. EXPERIMENTAL RESULTS

Successful cQED operation in this hardware is demonstrated with measurements of coherence times and interactions between each quantum object of the MMIQC. Measurements of the relevant coherence times in the device are shown in Figs. 3(a) and 3(b) and summarized in Table I. The qubit $T_1 = 6.4$ μs is on the order of other 3D transmons recently produced on silicon substrate in the same facility with similar methods [23] and $T_2^{\text{echo}} \approx 1.8T_1$. The thermal population of the qubit excited state is $< 3\%$. The micromachined cavity has a lifetime of 34.7 μs, which corresponds to a total quality factor $Q = 2 \times 10^6$ at single-photon energies.

Next, we find interaction strengths sufficiently large in relation to these coherences by showcasing some standard cQED functions. These measurements are shown in Figs. 3(c)–3(e). The dispersive coupling rate of the qubit to the readout cavity is $\chi_{qr}/2\pi = -3.84$ MHz, corresponding to the interaction strength $g/2\pi = 38$ MHz. In spectroscopy, we observe both resolved photon number splitting of the qubit [Fig. 3(a)] and a qubit-state-dependent shift of the micromachined cavity from a dispersive coupling rate $\chi_{q\mu}/2\pi = -1.17$ MHz. At detuning of $(\omega_q - \omega_\mu)/2\pi = -2.03$ GHz, this corresponds to $g/2\pi = 49$ MHz.

A final measurable parameter is the cross-Kerr interaction between the two cavities. The cavity cross-Kerr $\chi_{r\mu}$ is measured by the relative comparison of χ_{qr} and $\chi_{r\mu}$ [24]. A microwave pulse detuned 3 MHz above the readout cavity induces a Stark shift, which precedes single-sideband spectroscopy of both the qubit and micromachined cavity peaks. Both shift downward in frequency with the increasing power of the Stark pulse. The slopes of this response are proportional to χ_{qr} and $\chi_{r\mu}$, respectively [Fig. 3(b)]. We independently determine $\chi_{qr} = -3.84$ MHz by readout cavity spectroscopy with and without a preceding qubit π pulse. Finally, we find the cross-Kerr interaction $\chi_{r\mu}/2\pi = -20$ kHz, compared to a simulated value of -4.4 kHz.

As a further demonstration of the micromachined cavity's utility as a quantum memory, we perform Ramsey interferometry following a displacement that initializes the micromachined cavity to a coherent state of $|\beta\rangle$ with an average of three photons [Fig. 3(c)]. In this experiment, we

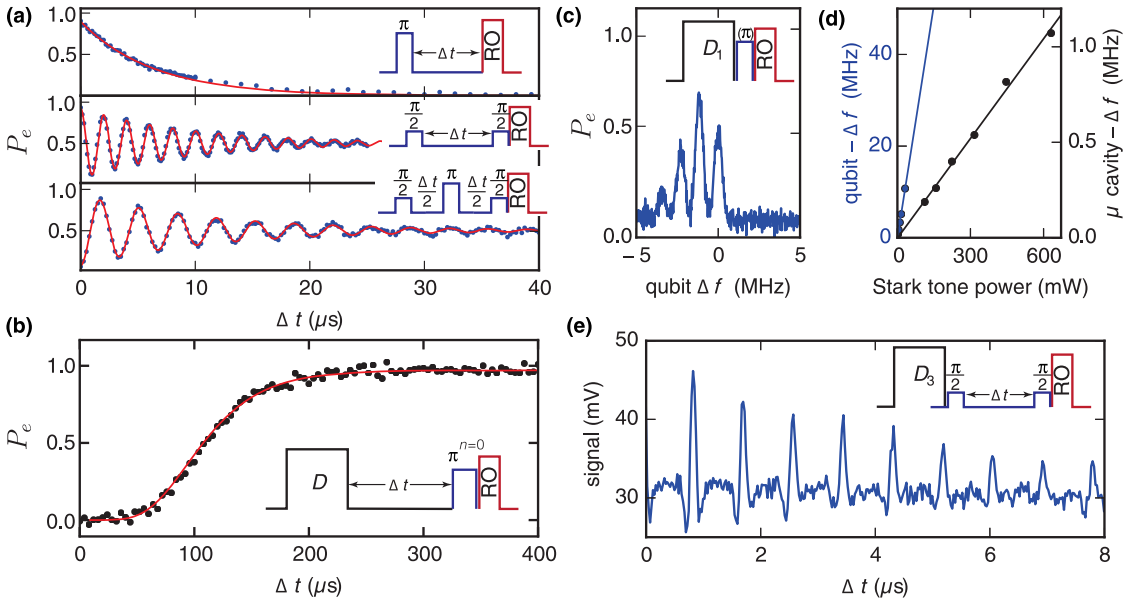

FIG. 3. (a) Qubit energy relaxation is fit to a single exponential (red line) with $T_1 = 6.4\ \mu$s. P_e is the probability that the qubit is measured in the excited state during a read-out (RO) pulse.. Ramsey dephasing time $T_2^R = 9.5\ \mu$s, measured here using 400-kHz detuning from the qubit frequency. Using a Hahn echo sequence, we find $T_2^{\text{echo}} = 11.7\ \mu$s, measured here using 300-kHz detuning from the qubit frequency. (b) Energy decay of the micromachined cavity is measured by applying a large displacement to this cavity, followed by a variable delay, followed by a spectrally narrow selective π rotation of the qubit conditioned on there being no photons in the readout cavity ($n = 0$). Using a Poissonian decay fit (red line), we find $T_1 = 34.7\ \mu$s. At 9.4 GHz, this decay time corresponds to a quality factor $Q = 2 \times 10^6$. (c) We observe number splitting of the qubit in spectroscopy after displacing the micromachined cavity by one photon. The spacing between the peaks indicates $\chi_{q\mu}/2\pi = 1.17$ MHz. (d) A tone detuned 3 MHz above the readout cavity induces a Stark shift that affects both the qubit and micromachined cavity frequencies. We use the ratio of these slopes $\chi_{qr}/\chi_{r\mu}$ to determine $\chi_{r\mu}$. (e) In Ramsey interferometery following a displacement of the micromachined (storage) cavity, we observe revivals of the qubit state occurring at integer multiples of $2\pi/\chi_{q\mu} = 0.855\ \mu$s [22].

prepare an initial state $|\beta_\mu\rangle \otimes \{|g\rangle + |e\rangle\}$, which precesses according to $e^{i\chi_{q\mu}ta^\dagger a|e\rangle\langle e|}$ [22]. Qubit-state revivals occur at time intervals $2\pi/\chi_{q\mu}$, consistent with our spectroscopic measurements of $\chi_{q\mu}$.

TABLE I. Measured device parameters. The cross-Kerr interaction with the qubit mode is denoted χ_q, and anharmonicity is α. Simulated parameters are in square brackets, and all other parameters are measured except the anharmonicities of the cavities, which are calculated by $\alpha = \chi_q^2/4\alpha_q$ [21].

Mode	Readout cavity	Transmon	μ-machined cavity
Frequency (MHz)	6973.4	7351.4	9377.2
[simulated]	[6945.1]	[7322.0]	[9258.0]
$\alpha_i/2\pi$ (MHz)	−0.012	−209.8	−0.002
[simulated]	[−0.004]	[−204.3]	[−0.002]
$\chi_{qi}/2\pi$ (MHz)	−3.84	···	−1.17
[simulated]	[−3.22]	···	[−1.25]
$\chi_{ri}/2\pi$ (MHz)	···	···	−0.020
[simulated]	···	···	[−0.004]
T_1 (μs)	1.0	6.4	34.3
T_2^R (μs)	···	9.5	···
T_2^{echo} (μs)	···	11.7	···

V. DISCUSSION OF LOSS MECHANISMS

We assess several potential loss mechanisms that could be limiting the coherence times in our device. All quantum circuits are subject to sources of loss associated with packaging and assembly that become more severe as complexity increases [8]. For example, loss occurs at seams where there is finite conductance g_{seam} and nonzero admittance to surface currents y^i_{seam}, which may limit a mode i's coherence time to $T_1 = g_{\text{seam}}/y^i_{\text{seam}}\omega_i$. In the multilayer architecture, these seams are present in the bonds between layers and interfaces between different materials.

In this device, there are two types of seams that could contribute to loss. The first consists of In—In bonds at the perimeter of the cavities. Using simulated surface currents, we calculate the admittance in the micromachined cavity mode to be $y^\mu_{\text{In-In}} = 16.0\,\Omega^{-1}\,\text{m}^{-1}$. For the qubit mode, $y^q_{\text{In-In}} = 0.02\,\Omega^{-1}\,\text{m}^{-1}$, which is smaller because the surface currents are localized away from the In—In bond. Using the technique developed in Ref. [9], we are able to achieve an In—In bond conductance in our devices of $g_{\text{In-In}} \approx 10^8\,\Omega^{-1}\,\text{m}^{-1}$. If this were the only source of loss, it would limit the micromachined cavity to lifetime 100 μs. The second type of seam is a Al-Au-In transition in a 3 × 3-mm

square shape around the Al aperture transmon region. Using simulated surface currents, we calculate the admittances in the micromachined cavity and qubit mode: $y^{\mu}_{\text{Al-Au-In}} = 0.17\,\Omega^{-1}\,\text{m}^{-1}$ and $y^{q}_{\text{Al-Au-In}} = 0.52\,\Omega^{-1}\,\text{m}^{-1}$. Independent measurements of stripline resonators fabricated with like procedures show that $g_{\text{Al-Au-In}} \approx 4.2 \times 10^5\,\Omega^{-1}\,\text{m}^{-1}$ [13]. The resulting limitation on the qubit mode lifetime is $T_1 < g_{\text{seam}}/y^{q}_{\text{seam}}\omega_q \approx 20\ \mu\text{s}$. Limitation on the cavity-mode lifetime due to this seam is $T_1 \approx 40\ \mu\text{s}$.

We also verify that qubit and micromachined cavity lifetimes are not limited by the Purcell effect due to the overcoupled readout cavity. We simulate that the upper bounds to the qubit and micromachined cavity lifetimes due to this effect are 200 and 500 μs, respectively. In design, the Purcell limit of the micromachined cavity is mitigated by minimizing the area of the annular opening created by the aperture transmon between cavities.

Also present here are surface dielectric and conductor loss mechanisms that are broadly studied in superconducting circuits. The particular shapes of the electrodes in Fig. 2(c) are designed to minimize dielectric loss near the surface of the electrodes. The aperture transmon has smooth edges that are easily parametrized for optimization that includes consideration of surface participation ratios [13,16].

VI. OUTLOOK

The device presented here demonstrates the integration of a transmon with a superconducting micromachined cavity, forming a simple MMIQC. The coherence times and coupling rates are in the strong dispersive regime of cQED, enabling many quantum manipulations that are the precursor to large-scale quantum information processing.

We remark that this achievement was made without extensive fabrication optimization using industrial scale tools, indicating process robustness and the potential for improvement. For example, it is expected that surface cleaning will improve $g_{\text{Al-Au-In}}$, a seam conductance relevant to both the qubit and cavity modes. Alternative MMIQC designs are being developed that contain different seams and minimize the use of normal metals like gold. Extended qubit lifetimes can be achieved by the removal of the silicon substrate in the junction area and improved surface cleaning [23]. Furthermore, a wide range of coupling rates can be accessed by geometry modifications, some of which would require precise alignment and leveling control during wafer bonding.

We have shown a proof-of-principle MMIQC that demonstrates the engineering of qubit-cavity coupling. There are numerous possible next steps using the design strategies and fabrication tools described in this work. For instance, the micromachined cavity and qubit can be addressed using microstrips on the side of the wafer opposite to the micromachined cavity wall and qubit fabrication, eliminating the machined readout cavity. They can function as planar readout resonators and incorporate Purcell filtering [25,26]. As a further example, the addition of a second junction and flux-bias line would constitute a frequency tunable device inspired by the concentric transmon in Ref. [27]. More sophisticated on-chip input-output circuitry, such as quantum limited amplifiers [28–30], circulators [31,32], and switching elements [33,34], will also be required for practical quantum information processing. This integration will likely be accompanied by through-wafer metallized vias to prevent cross talk. As this multilayer structural architecture is further developed, we expect to see multiqubit-multicavity devices of schemes similar to and extending beyond those currently implemented in either planar or 3D cavity architectures. We anticipate that the techniques demonstrated here can be successfully employed toward integrating these elements into increasingly complex MMIQCs.

ACKNOWLEDGMENTS

We thank Zlatko Minev, Kyle Serniak, Ioan Pop, Michel H. Devoret, Hanhee Paik, and David Pappas for useful conversations, Subhajyoti Chaudhuri for assistance with simulations, and Jan Schroers and Emily Kinser for assistance with wafer bonding. This research was supported by the U.S. Army Research Office under Grant No. W911NF-14-1-0011. W. P. was supported by NSF Grant No. PHY1309996 and by a fellowship instituted with a Max Planck Research Award from the Alexander von Humboldt Foundation. C. A. acknowledges support from the NSF Graduate Research Fellowship under Grant No. DGE-1122492. Facilities use was supported by the Yale SEAS cleanroom, YINQE, and NSF MRSEC DMR-1119826.

[1] L. P. B. Katehi, J. F. Harvey, and K. J. Herrick, 3-D integration of RF circuits using Si micromachining, IEEE Microw. Mag. **2**, 30 (2001).

[2] J. H. Béjanin, T. G. McConkey, J. R. Rinehart, C. T. Earnest, C. R. H. McRae, D. Shiri, J. D. Bateman, Y. Rohanizadegan, B. Penava, P. Breul, S. Royak, M. Zapatka, A. G. Fowler, and M. Mariantoni, Three-Dimensional Wiring for Extensible Quantum Computing: The Quantum Socket, Phys. Rev. Applied **6**, 044010 (2016).

[3] A. R. Brown, P. Blondy, and G. M. Rebeiz, Microwave and millimeter-wave high-Q micromachined resonators, Int. J. RF Microwave Comput. Aid. Eng. **9**, 326 (1999).

[4] L. P. Katehi, Office of Naval Research Final Report No. 033095-1-F, 1997.

[5] S. K. Tolpygo, Superconductor digital electronics: Scalability and energy efficiency issues (review article), Low Temp. Phys. **42**, 361 (2016).

[6] S. K. Tolpygo, V. Bolkhovsky, T. Weir, L. M. Johnson, W. D. Oliver, and M. A. Gouker, Deep sub-micron stud-via technology of superconductor vlsi circuits, Supercond. Sci. Technol. **27**, 025016 (2014).

[7] D. Bintley, M. J. MacIntosh, W. S. Holland, J. T. Dempsey, P. Friberg, J. T. Kuroda, E. G. Starman,

H. S. Thomas, C. Walther, X. Gao, P. A. R. Ade, R. V. Sudiwala, C. Dunare, W. Parkes, A. J. Walton, K. D. Irwin, G. C. Hilton, M. Niemack, M. Amiri, V. Asboth, B. Burger, E. L. Chapin, M. Halpern, M. Hasselfield, and A. L. Woodcraft, Scaling the summit of the submillimetre: Instrument performance of SCUBA-2, in *SPIE Astronomical Telescopes+Instrumentation*, edited by W. S. Holland, SPIE Proceedings Vol. 8452 (SPIE–International Society for Optical Engineering, Bellingham, WA, 2012), p. 845208.

[8] T. Brecht, W. Pfaff, C. Wang, Y. Chu, L. Frunzio, M. H. Devoret, and R. J. Schoelkopf, Multilayer microwave integrated quantum circuits for scalable quantum computing, npj Quantum Inf. **2**, 16002 (2016).

[9] T. Brecht, M. Reagor, Y. Chu, W. Pfaff, C. Wang, L. Frunzio, M. H. Devoret, and R. J. Schoelkopf, Demonstration of superconducting micromachined cavities, Appl. Phys. Lett. **107**, 192603 (2015).

[10] H. Paik, D. I. Schuster, L. S. Bishop, G. Kirchmair, G. Catelani, A. P. Sears, B. R. Johnson, M. J. Reagor, L. Frunzio, L. I. Glazman, S. M. Girvin, M. H. Devoret, and R. J. Schoelkopf, Observation of High Coherence in Josephson Junction Qubits Measured in a Three-Dimensional Circuit QED Architecture, Phys. Rev. Lett. **107**, 240501 (2011).

[11] Z. K. Minev, K. Serniak, I. M. Pop, Z. Leghtas, K. Sliwa, M. Hatridge, L. Frunzio, R. J. Schoelkopf, and M. H. Devoret, Planar Multilayer Circuit Quantum Electrodynamics, Phys. Rev. Applied **5**, 044021 (2016).

[12] A. Blais, R.-S. Huang, A. Wallraff, S. M. Girvin, and R. J. Schoelkopf, Cavity quantum electrodynamics for superconducting electrical circuits: An architecture for quantum computation, Phys. Rev. A **69**, 062320 (2004).

[13] See Supplemental Material at http://link.aps.org/supplemental/10.1103/PhysRevApplied.7.044018 for additional details pertaining to coupling trends, fabrication, transmon geometry, and loss analysis, which includes Refs. [14–18].

[14] J. D. Jackson, *Classical Electrodynamics*, 3rd ed. (Wiley, New York, 1998).

[15] R. E. Collin, *Field Theory of Guided Waves*, 2nd ed. (Wiley-IEEE Press, New York, 1990).

[16] C. Wang, C. Axline, Y. Y. Gao, T. Brecht, Y. Chu, L. Frunzio, M. H. Devoret, and R. J. Schoelkopf, Surface participation and dielectric loss in superconducting qubits, Appl. Phys. Lett. **107**, 162601 (2015).

[17] Q. Huang, G. Xu, Y. Yuan, X. Cheng, and L. Luo, Development of indium bumping technology through AZ9260 resist electroplating, J. Micromech. Microeng. **20**, 055035 (2010).

[18] W. Zhang and W. Ruythooren, Study of the Au/In reaction for transient liquid-phase bonding and 3D chip stacking, J. Electron. Mater. **37**, 1095 (2008).

[19] J. Koch, T. M. Yu, J. Gambetta, A. A. Houck, D. I. Schuster, J. Majer, A. Blais, M. H. Devoret, S. M. Girvin, and R. J. Schoelkopf, Charge-insensitive qubit design derived from the Cooper pair box, Phys. Rev. A **76**, 042319 (2007).

[20] J. A. Schreier, A. A. Houck, J. Koch, D. I. Schuster, B. R. Johnson, J. M. Chow, J. M. Gambetta, J. Majer, L. Frunzio, M. H. Devoret, S. M. Girvin, and R. J. Schoelkopf, Suppressing charge noise decoherence in superconducting charge qubits, Phys. Rev. B **77**, 180502(R) (2008).

[21] S. E. Nigg, H. Paik, B. Vlastakis, G. Kirchmair, S Shankar, L. Frunzio, M. H. Devoret, R. J. Schoelkopf, and S. M. Girvin, Black-Box Superconducting Circuit Quantization, Phys. Rev. Lett. **108**, 240502 (2012).

[22] B. Vlastakis, G. Kirchmair, Z. Leghtas, S. E. Nigg, L. Frunzio, S. M. Girvin, M. Mirrahimi, M. H. Devoret, and R. J. Schoelkopf, Deterministically encoding quantum information using 100-photon Schrodinger cat states, Science **342**, 607 (2013).

[23] Y. Chu, C. Axline, C. Wang, T. Brecht, Y. Y. Gao, L. Frunzio, and R. J. Schoelkopf, Suspending superconducting qubits by silicon micromachining, Appl. Phys. Lett. **109**, 112601 (2016).

[24] Z. Leghtas, S. Touzard, I. M. Pop, A. Kou, B. Vlastakis, A. Petrenko, K. M. Sliwa, A. Narla, S. Shankar, M. J. Hatridge, M. Reagor, L. Frunzio, R. J. Schoelkopf, M. Mirrahimi, and M. H. Devoret, Confining the state of light to a quantum manifold by engineered two-photon loss, Science **347**, 853 (2015).

[25] M. D. Reed, B. R. Johnson, A. A. Houck, L. DiCarlo, J. M. Chow, D. I. Schuster, L. Frunzio, and R. J. Schoelkopf, Fast reset and suppressing spontaneous emission of a superconducting qubit, Appl. Phys. Lett. **96**, 203110 (2010).

[26] C. Axline, M. Reagor, R. W. Heeres, P. Reinhold, C. Wang, K. Shain, W. Pfaff, Y. Chu, L. Frunzio, and R. J. Schoelkopf, An architecture for integrating planar and 3D cQED devices, Appl. Phys. Lett. **109**, 042601 (2016).

[27] J. Braumüller, M. Sandberg, M. R. Vissers, A. Schneider, S. Schlör, L. Grünhaupt, H. Rotzinger, M. Marthaler, A. Lukashenko, A. Dieter, A. V. Ustinov, M. Weides, and D. P. Pappas, Concentric transmon qubit featuring fast tunability and an anisotropic magnetic dipole moment, Appl. Phys. Lett. **108**, 032601 (2016).

[28] M. A. Castellanos-Beltran and K. W. Lehnert, Widely tunable parametric amplifier based on a superconducting quantum interference device array resonator, Appl. Phys. Lett. **91**, 083509 (2007).

[29] N. Bergeal, F. Schackert, M. Metcalfe, R. Vijay, V. E. Manucharyan, L. Frunzio, D. E. Prober, R. J. Schoelkopf, S. M. Girvin, and M. H. Devoret, Phase-preserving amplification near the quantum limit with a Josephson ring modulator, Nature (London) **465**, 64 (2010).

[30] C. Macklin, K. O'Brien, D. Hover, M. E. Schwartz, V. Bolkhovsky, X. Zhang, W. D. Oliver, and I. Siddiqi, A near–quantum-limited Josephson traveling-wave parametric amplifier, Science **350**, 307 (2015).

[31] K. M. Sliwa, M. Hatridge, A. Narla, S. Shankar, L. Frunzio, R. J. Schoelkopf, and M. H. Devoret, Reconfigurable Josephson Circulator/Directional Amplifier, Phys. Rev. X **5**, 041020 (2015).

[32] J. Kerckhoff, K. Lalumière, B. J. Chapman, A. Blais, and K. W. Lehnert, On-Chip Superconducting Microwave Circulator from Synthetic Rotation, Phys. Rev. Applied **4**, 034002 (2015).

[33] M. Pechal, J.-C. Besse, M. Mondal, M. Oppliger, S. Gasparinetti, and A. Wallraff, Superconducting Switch for Fast On-Chip Routing of Quantum Microwave Fields, Phys. Rev. Applied **6**, 024009 (2016).

[34] B. J. Chapman, B. A. Moores, E. I. Rosenthal, J. Kerckhoff, and K. W. Lehnert, General purpose multiplexing device for cryogenic microwave systems, Appl. Phys. Lett. **108**, 222602 (2016).